Aerodynamic optimization of the exhaust system of an aft-mounted boundary layer ingestion propulsor

Jesús Matesanz-García[1*], Tommaso Piovesan[1] David G. MacManus[1]

[1]*School of Aerospace, Transport and Manufacturing, Cranfield University, MK43 0AL, Bedfordshire, United Kingdom*
[*]*Corresponding author: Jesus.Matesanz-Garcia@cranfield.ac.uk*

Abstract

Purpose - Novel aircraft propulsion configurations require a greater integration of the propulsive system with the airframe. As a consequence of the closer integration of the propulsive system, higher levels of flow distortion at the fan face are expected. This distortion will propagate through the fan and penalize the system performance. This will also modify the exhaust design requirements. This paper proposes a methodology for the aerodynamic optimization of the exhaust for novel embedded propulsive systems. To model the distortion transfer, a low order throughflow fan model is included.

Design/methodology/approach - As the case study a 2D axisymmetric aft-mounted annular boundary layer ingestion (BLI) propulsor is used. An automated CFD approach is applied with a parametric definition of the design space. A throughflow body force model for the fan is implemented and validated for 2D axisymmetric and 3D flows. A multi-objective optimization based on evolutionary algorithms is used for the exhaust design.

Findings - By the application of the optimization methodology, a maximum benefit of approximately 0.32% of the total aircraft required thrust was observed by the application of compact exhaust designs. Furthermore, for the embedded system, is observed that the design of the compact exhaust and the nacelle afterbody have a considerable impact on the aerodynamic performance.

Originality - This paper presents a novel approach for the exhaust design of embedded propulsive systems in novel aircraft configurations. To the author's knowledge, this is the first detailed optimization of the exhaust system on an annular aft-mounted BLI propulsor.

Keywords Multi-objective optimization, exhaust system, boundary layer ingestion, coupled aerodynamics

1. Introduction

Several novel aircraft propulsion configurations have been proposed in recent times to mitigate the environmental impact of the aviation (Dae Kim 2010, Gohardani et al. 2011, Steiner et al. 2012, Wiart et al. 2015). A shared feature between these configurations is the increase of the integration between the propulsive system and the airframe, with the intrinsic increase of the aerodynamic coupling. The increase of the aerodynamic coupling implies that the importance of the propulsion integration on the overall aerodynamic performance will increase with respect to conventional podded configurations. Therefore, it becomes essential to evaluate the impact of the different housing components (intake, nacelle, and exhaust) of the propulsion integration of such novel aircraft configurations from early design stages.

A consequence of the rise in the aerodynamic coupling is a closer interaction between the housing components of the propulsion integration. This interaction requires an integrated design methodology (Matesanz-García et al. 2020). Moreover, the greater integration of the propulsor with the airframe is expected to increase the flow distortion levels at the intake. This flow distortion will propagate through the turbomachinery and penalize the overall system performance (Defoe et al. 2018, Gunn et al. 2013). The aerodynamic design of the exhaust system becomes critical, since small penalties on the exhaust performance can lead to higher specific fuel consumption in low specific thrust engines (Goulos et al. 2016). In addition, the total pressure, total temperature and swirl profiles at the propulsor exit are expected to have an impact on the exhaust design requirements (Goulos et al. 2019, Lee et al. 2018).

It is therefore necessary to model the distortion transfer through the propulsor to accurately evaluate the propulsion integration of novel embedded propulsive systems. For a coupled system, the computational cost of a direct simulation of the turbomachinery stage can be prohibitive. This will reduce the extent of the studies that can be carried for close-coupled propulsive systems. To address this issue, different lower fidelity approaches have been proposed to model the turbomachinery effects of the embedded systems. Simplified one-dimensional turbomachinery models have been used in boundary layer ingestion studies as Habermann et al. (2020) and Matesanz-García et al. (2020). Two-dimensional and quasi-2D turbomachinery models have also been applied. Habermann et al. (2021) defined a normalized pressure and temperature jump based on inlet profiles. Lee et al. (2018) modified a quasi-2D throughflow method as part of a multi-fidelity approach for the design of a BLI propulsor. Actuator disk models have been also applied for turbomachinery modelling in embedded systems in works such as Lee et al. (2020) and Hall et al. (2017). Higher fidelity volume based approaches such as body force models (BFM) have been also used for this purpose. Seitz et al. (2020) included an axisymmetric definition of the body forces to model the total pressure rise neglecting the swirl effects within an optimization framework for an aft mounted annular BLI propulsor. Kim & Liou (2017) developed a three-dimensional body force model formulation based on the entropy production to model the losses of the turbomachinery to optimize the propulsive system of

a blended-wing-body configuration. Also, Lee et al. (2018) applied the same BFM as part of their multi-fidelity propulsor design approach. Other BFM have been proposed to model close-coupled propulsive systems. An inviscid Body Force Model based on the discrete turbomachinery element was originally proposed by Hall (2015). That approach was used to model boundary layer ingestion effects on the turbomachinery performance by Defoe et al. (2018). Hall's formulation was modified for viscous flows with an explicit formulation of the turbomachinery losses and compressibility effects by Thollet (2017). This approach was utilized to model the turbomachinery performance of an embedded system by Benichou et al. (2019).

It is crucial to develop robust design methodologies for the exhaust system of the close-coupled configurations from an early design stage. These methodologies should include the intake distortion transfer through the turbomachinery and account for the influence of the nacelle design on the exhaust flow. The performance of the turbomachinery, the exhaust and the general propulsion system must be analyzed to account for these effects. Hence, a robust throughflow method is required. In the present work, the turbomachinery is modelled with the Hall-Thollet (Thollet 2017) throughflow model. A validation of the model against the NASA Rotor 4 (Hughes 2002) geometry is provided for 2D axisymmetric and 3D flow applications.

The aim of the present work is to define a methodology for the optimization of exhaust systems for novel embedded propulsive systems. A 2D axisymmetric aft mounted annular boundary layer ingestion fuselage based on a medium-range single-aisle aircraft is applied as the case study. An automated CFD approach is used with a parametric definition of the design space. A multi-objective optimization based on evolutionary algorithms is proposed for the exhaust design optimization. The metrics of interest are selected through an analysis of their influence on the system performance. To the author's knowledge, this is the first detailed optimization of an exhaust system on an annular aft-mounted BLI propulsor.

2. Methodology

2.1. Aerodynamic design

An intuitive Class-Shape Transformation (iCST) method (Christie et al. 2019) is applied for the construction of the aerodynamic surfaces of the propulsion integration. This method defines complex aerodynamic geometries through a reduced number of parameters. The parametrization applied in the present work is based on the defined by Matesanz-García et al. (2020). This parametrization allows the independent definition of the propulsion integration housing components and the general propulsor axial and radial location based on an elliptical nose axisymmetric reference fuselage (Fig. 1).

The aft-fuselage, the intake, and the exhaust upper and lower geometries are defined by a single independent iCST curve. The fan-cowl design is split at the maximum radius point between two iCST curves for the forebody and the afterbody. The forebody curve is defined to be independent of the afterbody geometry. The curvature at the maximum radius location will be obtained automatically to minimize the rate of radius of curvature

along the forebody. This curvature constraint will be enforced on the afterbody iCST. Hence, for a given forebody geometry the afterbody geometry can vary freely based on the trailing edge radial location, r_{te}, the length of the nacelle, l_{nac}, and the boat-tail angle, β_{nac}.

The propulsor domain (FAN and OGV) is defined from the reference fan configuration of the study (Hughes 2002). The domain is extended by 10% of the blade chord upstream of the foremost fan blade coordinate and 10% of the blade chord from the aftmost vane coordinate. The hub-to-tip ratio is kept constant. To match the geometry transition from the aft fuselage curve, the intake and the exhaust geometries to the propulsor domain, a second order iCST curve is applied based on the local slope constraints (θ_{ff}, β_{int}, $\theta_{up_{noz}}$, and $\theta_{down_{noz}}$). A rolling ball method is used to define the intake and exhaust area constraints (A_{thr} and A_{noz}).

2.2. Performance evaluation

2.2.1. Modified near-field method

A modified near-field method based on the AGARD 237 (MIDAP Study group 1979) is applied for the force bookkeeping of the configuration (Fig. 2). The approach has been adapted to account for the embedded propulsor requirements (Matesanz-García et al. 2020). The forces are split into three groups: the surface forces (Equation 1), θ_i; the gauge forces (Equation 2), F_i; and the drag forces (Equation 3), ϕ_i. This last group includes three distinct forces: the pre-entry drag, ϕ_{pre}; the cowl drag, ϕ_{nac}; and the post-exit drag ϕ_{post}. The pre-entry drag force (Equation 4) is derived from a momentum balance applied to the inlet capture volume (Fig. 2). The upstream gauge force, F_{G0}, is defined by the mass flow rate of the propulsive system and the ambient operation conditions. The split between the nacelle and intake surface forces is defined by the stagnation point. This point is located where the axial wall shear stress changes polarity on the cowl lip surface.

$$\theta_i = \int \left[(p - p_\infty) + \tau_{wall,x} \right] dA \tag{1}$$

$$F_i = \int \left[(p - p_\infty) + V_x \left(\rho \mathbf{V} \cdot \mathbf{n} \right) \right] dA \tag{2}$$

$$\phi_i = -\theta_i \tag{3}$$

$$\phi_{pre} = -F_{G0} + F_{F,F} + \theta_{Intake} + \theta_{fus} \tag{4}$$

The modified drag and thrust forces are defined by excluding ϕ_{post} (Eqs. 5-6). The modified thrust force is obtained from the balance of the modified Gross Propulsive Force (Equation 7), GPF^*, and the upstream gauge force. To obtain the force balance of the Gross Propulsive force (Equation 8), GPF, the post-exit drag terms are included. This force term is obtained by the integration of the pressure forces over a streamline from the nacelle trailing edge. The modified drag and thrust forces are used to define the Net Vehicle Force (Equation 9), NVF. This term accounts for the full force balance on the aircraft and the propulsion integration.

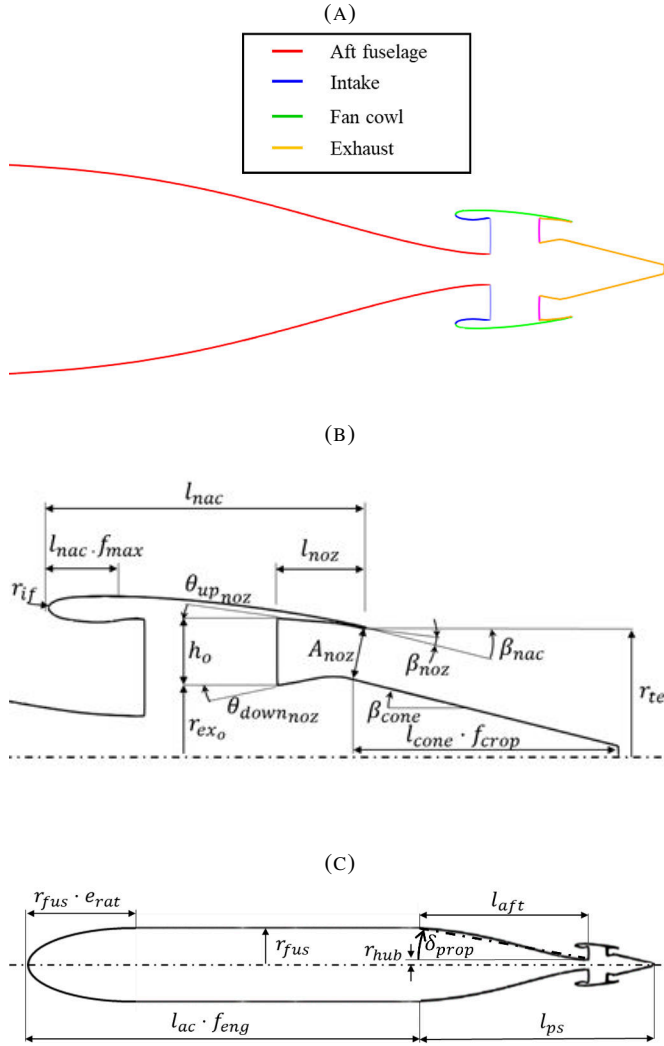$$D^* = \phi_{pre} + \phi_{nac} \tag{5}$$

FIGURE 1: Geometry parameterization: (a) housing components definition, (b) fan cowl and exhaust parameters, and (c) fuselage geometry parameters and system location, not to scale

$$T^* = -F_{G0} + GPF^* \tag{6}$$

$$GPF^* = F_{OGV} - \theta_{nozzle,up} - \theta_{nozzle,down} - \theta_{cone} \tag{7}$$

$$GPF = GPF^* + \phi_{post} \tag{8}$$

$$NVF = D^* - T^* \tag{9}$$

2.2.2. *Normalized performance analysis*

The NVF defines the balance between thrust and drag forces on the system. However, this force balance does not define the benefit of the propulsion integration design. To
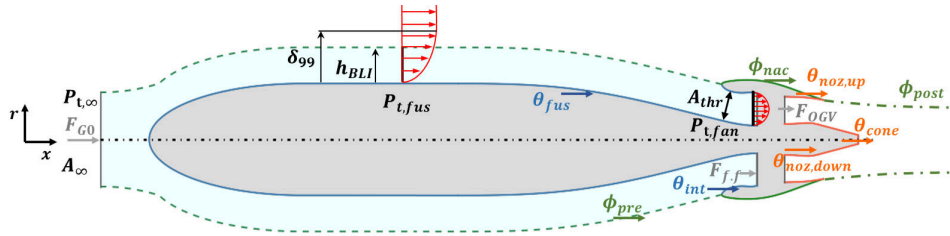
FIGURE 2: Modified Near-Field method domain and forces. Definition of the reference stations on the fuselage and the fan face

address this, the force bookkeeping can be normalized based on the NVF of the reference aircraft without the embedded propulsive system (Valencia et al. 2015, Sanders 2018). A reference axisymmetric fuselage based on the sideline of the baseline aircraft is used for this purpose. Then, the Relative Net Thrust force (Equation 10), F_{RN}, is defined as the benefit of the integration of the new embedded propulsor. The F_{RN} can be scaled with the reference required thrust of the baseline aircraft, T_{ref}, to define the Thrust Split (Equation 11), TS. The TS defines the fraction of the total thrust requirement that is provided by the embedded propulsor integration. To account for the propulsor performance, the Thrust Specific Power Consumption (Equation 12), $TSPC$, is defined by the normalization of the propulsor power input W_{prop} with the F_{RN}. The W_{prop} is obtained as the enthalpy balance between the fan face and the OGV exit.

$$F_{RN} = NVF - NVF_{ref-ac} \tag{10}$$

$$TS = -\frac{F_{RN}}{T_{ref}} \tag{11}$$

$$TSPC = -\frac{W_{prop}}{F_{RN}} \tag{12}$$

2.2.3. *Exhaust performance*

Non dimensional coefficients are applied for the definition of the exhaust performance based on the work of Goulos et al. (2016). The coefficients are the discharge coefficient, C_D, and the velocity coefficient, C_V. The discharge coefficient (Equation 13), is defined as the ratio between the actual mass flow at the exhaust duct and the ideal isentropic mass flow though the exhaust nozzle throat (Equation 14). The velocity coefficient (Equation 15) is defined as the ratio between the Gross Propulsive Force and the Ideal Propulsive Force (Equation 16), IPF. The IPF is defined based on the ideal velocity at the exhaust nozzle throat (Equation 17) and the actual mass flow through the exhaust.

$$C_D = \frac{\dot{m}_{actual}}{\left(\frac{\dot{m}}{A}\right)_{ideal} A_{noz}} \tag{13}$$

$$\left(\frac{\dot{m}}{A}\right)_{ideal} = P_t \left(\frac{1}{\lambda}\right) \sqrt{\frac{2\gamma}{(\gamma-1) R T_t} \left(1 - \left(\frac{1}{\lambda}\right)^{\frac{\gamma-1}{\gamma}}\right)} \tag{14}$$

$$C_V = \frac{GPF}{IPF} \tag{15}$$

$$IPF = \dot{m}_{actual} \cdot V_{ideal} \tag{16}$$

$$V_{ideal} = \sqrt{\frac{2\gamma R T_t}{(\gamma - 1)} \left(1 - \left(\frac{1}{\lambda}\right)^{\frac{\gamma-1}{\gamma}}\right)} \tag{17}$$

The reference metrics (Equation 14-17) are obtained from the mass weighted average values of the total pressure and total temperature at the exhaust duct. The nozzle pressure ratio, λ, is defined as the ratio between the mass averaged total pressure at the exhaust and the ambient static pressure. The reference ambient static pressure is defined by the operating altitude. For the isentropic mass flow (Equation 14) definition if $\lambda \geq \lambda_{crit} = ((\gamma + 1)/2)^{\frac{\gamma}{\gamma-1}}$ the value is set to λ_{crit}, while the real value of λ is used for the ideal velocity (Equation 17). Another metric of interest is the effective nozzle pressure ratio, λ_{eff}. This metric is defined as the nozzle pressure ratio, but the static value of reference is the effective value at the exhaust discharge plane. This value normally differs from the ambient static pressure reference and the difference is expected to increase on embedded propulsion systems due to the impact of the aerodynamic coupling between the airframe and the propulsion integration.

2.3. Turbomachinery model

The turbomachinery is modelled using the Hall-Thollet low order method (Thollet 2017). This formulation is based on the substitution of the discrete turbomachinery elements by source terms on the Navier-Stokes equations. The source terms are formulated in a flow relative reference frame with two main components: the normal body force, f_n, and the parallel body force, f_p (Fig. 3). The normal force is responsible of the generation of the main turning of the flow, and the parallel force is responsible of the generation of the losses of the turbomachinery. These components are projected to the absolute frame of reference and added to the main flow equations (Eqs. 18-20). The metal blockage effect (Fig. 3) is modelled with the blockage factor (Equation 21).

$$\frac{\partial \rho}{\partial t} + \nabla \cdot (\rho \mathbf{V}) = -\frac{1}{b} (\rho \mathbf{V} \cdot \nabla b) \tag{18}$$

$$\frac{\partial \rho \mathbf{V}}{\partial t} + \mathbf{V} \cdot \nabla \mathbf{V} - \nabla \cdot \bar{\bar{\tau}} = \rho \mathbf{f} - \frac{1}{b} (\rho \mathbf{V} \cdot \nabla b) \mathbf{V} \tag{19}$$

$$\frac{\partial \rho e_t}{\partial t} + \nabla \cdot \left(\rho h_t \mathbf{V} - \bar{\bar{\tau}} \cdot \mathbf{V}\right) = \rho \Omega f_\theta - \frac{1}{b} (\rho h_t \mathbf{V} \cdot \nabla b) \tag{20}$$

$$b = N_{blades} \frac{\theta_{ps} - \theta_{ss}}{2\pi} \tag{21}$$

Hall's BFM (Hall 2015) included a normal force definition for an inviscid and incompressible flow formulation (Equation 22). This model provides the theoretical lift coefficient of an isolated flat plate for the blade and it is consistent with the behaviour in the infinite solidity limit. This formulation in based on the explicit definition of the flow
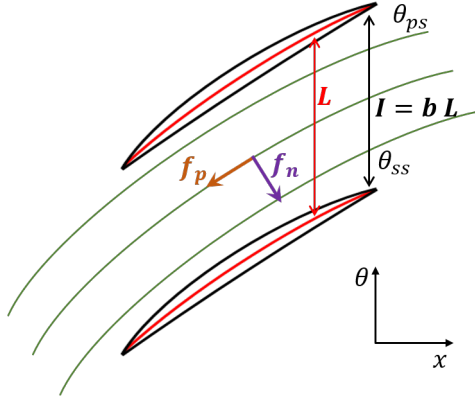
FIGURE 3: Representation of the relative components of the flow source terms compared with the blade generated flow turning, and definition of the metal blockage terms

turning with the normal force (f_n), and does not have additional calibration terms. The flow turning is a result of the blade geometry and local flow conditions. The formulation of the normal force depends on the normal vector to the blade and vane camber angles, $\mathbf{n}$; the local pitch , s (Equation 23); the local deviation angle, δ (Equation 24); and the local relative velocity magnitude, W (Equation 25).

$$f_n = 0.5 \frac{W^2 2\pi\delta}{s\,|n_\theta|} \tag{22}$$

$$s = \frac{2\pi r}{N_{blades}} \tag{23}$$

$$\delta = arcsin\left(\frac{\mathbf{W} \cdot \mathbf{n}}{|\mathbf{W}|}\right) \tag{24}$$

$$\mathbf{W} = \mathbf{V} - \Omega r \cdot \mathbf{e}_\theta \tag{25}$$

Thollet (2017) proposed a compressible and viscous approach of Hall's BFM by the addition of a blockage and compressibility correction, as well as a parallel force definition to model the blade loses. The compressibility correction is based on the Prandtl-Gauert correction for the incompressible regime and an Ackeret formulation for the supersonic regime. The compressibility effect is included to the normal (Equation 26) and parallel force (Equation 27) components by a compressibility correction factor, K_{Mach} (Equation 28). To model the losses Thollet defines two main loss sources. The first source models the losses with a simple friction coefficient correlation for a turbulent flow flat plate (Equation 29). The second is a calibration term to match the maximum efficiency point location by the selection of a reference point for the calibration deviation angle.

To define the body forces orientation, the plane containing the local relative velocity vector and the local blade normal is first defined. Then the normal force component must be orthogonal to the normal of this plane and to the parallel force component. Since the parallel force component is defined to be oriented against the relative velocity (Equation

30), the normal force must be orthogonal to both the normal to the plane and the relative velocity vector (Equation 31).

$$f_n = \frac{K_{Mach}0.5W^2 2\pi\delta}{sb\,|n_\theta|} \tag{26}$$

$$f_p = \frac{0.5W^2}{sb\,|n_\theta|}\left(2C_f + 2\pi K_{Mach}\left(\delta - \delta^{\eta_{cal}}\right)^2\right) \tag{27}$$

$$K_{Mach} = \begin{cases} min\left(\frac{1}{\sqrt{1-M_r^2}}, 3\right), & if\ M_r < 1 \\ min\left(\frac{1}{2\pi\sqrt{M_r^2-1}}, 3\right), & if\ M_r > 1 \end{cases} \tag{28}$$

$$C_f = 0.0592 Re_x^{-0.2} \tag{29}$$

$$\frac{\mathbf{f_p}}{|\mathbf{f_p}|} = \frac{\mathbf{W}}{|\mathbf{W}|} \tag{30}$$

$$\frac{\mathbf{f_n}}{|\mathbf{f_n}|} = \mathbf{W} \times (\mathbf{W} \times \mathbf{n}) \tag{31}$$

2.4. CFD methodology

Favre-averaged Navier-Stokes equations with the k-ω SST turbulence closure model are used for the CFD approach. A second-order upwind scheme is used for the cell discretization and a Green-Gaus Cell-based method is applied for gradient computation. The fluid properties are defined with the kinetic theory and the a real gas model. Sutherland's Law is used to adjust the viscosity with the temperature. A 2D axisymmetric multi-block mesh is applied with a y^+ value of one. The CFD methodology was validated for transonic bodies of revolution by Milea (2020), for fan cowl aerodynamics by Tejero et al. (2022), and for exhaust aerodynamics by Goulos et al. (2016).

A C-shape domain is used. The flight operating conditions are defined by far-field boundary conditions based on the flight Mach number and altitude. No-slip adiabatic walls are used for the definition of the aerodynamic surfaces. The Hall-Thollet BFM is applied to model the propulsor contribution. An axisymmetric swirl component is applied to model the flow turning effects (ANSYS INC 2019). The numerical uncertainty of the model is obtained based on the approach defined by Celik et al. (2008). Three meshes with progressive refinements are compared (4×10^5, 7×10^5, and 1.3×10^6). The intermediate mesh (7×10^5) was selected to reduce the computational cost. A GCI value of 0.004% and 0.015% was obtained for the C_V and C_V^*, respectively. The GCI for the C_D is 0.051%. The NVF and the W_{prop} GCIs were 0.521% and 0.354%, respectively. The evaluation of the uncertainty of the TS and $TSPC$ requires to include the uncertainty on the NVF_{ref-ac}. Thus, a grid sensitivity study was carried for the reference axisymmetric fuselage configuration with three mesh refinements (134×10^3, 446×10^3, and 1.481×10^4). The finest mesh was selected as the reference with a GCI of 0.011% on the NVF_{ref-ac}. The cumulative error is then obtained by quadrature (Taylor 1997). This results in an uncertainty of of $\pm 1.925 \times 10^{-5}$ units for the TS ($\sim$ 0.002% of the total thrust required), and $\pm 1.953\,m/s$ for the $TSPC$. In the exhaust performance metrics, the

uncertainty from the mesh is $\pm 4.03 \times 10^{-5}$ units, $\pm 1.53 \times 10^{-5}$ units, and $\pm 5.05 \times 10^{-5}$ units for the C_V, C_V^*, and the C_D, respectively. With this mesh resolution, each CFD evaluation has an approximate cost of 10 CPU hours (hour $\times$ CPU) and it is run with 20 CPUs.

3. Body force model validation

In an embedded propulsive system, such as the aft-mounted BLI propulsor, significant levels of intake distortion are expected (Gunn et al. 2013, Defoe et al. 2018). The intake distortion will propagate through the fan stage and change the exhaust design operating conditions. Thus, a representative through-flow fan model is required to evaluate the aerodynamic performance of the embedded propulsor. However, the computational cost required for a direct simulation of the fan stage is prohibitive for some design activities (e.g. design space exploration and optimisation). Low order methods, such as the Hall-Thollet (Thollet 2017) body force model, can be used to reduce the computational cost while maintaining an adequate representation of the flow at the fan stage. This approach is coupled with a compressible, viscous CFD methodology. In comparison with a higher fidelity reference, some loss in the accuracy is expected. Nevertheless, in the preliminary design of the exhaust system of the aft-mounted propulsor, a low order model will suffice if the bulk characteristics of the flow at the fan stage are captured (i.e. FPR, η_{is}, and radial distributions of total temperature). A validation of the Hall-Thollet (Thollet 2017) low order turbomahinery model is performed to understand the applicability of this low order fan approach.

The implementation of the Hall-Thollet (Thollet 2017) low order turbomahinery model into the ANSYS Fluent (ANSYS INC 2019) framework was validated for the NASA Rotor 4 (R4) configuration (Hughes 2002). The NASA R4 is a scaled single stage configuration based on a medium pressure-ratio, high bypass-ratio turbofan (Table 1). For the validation process the measure stations of the reference metrics are based on the experimental reference (Fig. 4) (Hughes 2002, Hughes et al. 2013).

Rotor 4 design characteristics	
N_{blades}	22
N_{vanes}	54
Fan tip diameter	0.65 m
httr	0.3
Corrected RPM (100%)	12,657
Stage PR	1.47
Tip relative Mach number	1.26

TABLE 1

NASA Rotor 4 design characteristics (Hughes 2002)

3.1. *CFD methodology for the validation*

The BFM implementation was validated for 3D and 2D axisymmetric flows. For the 2D axisymmetric a meridional cut of the intake, stage and exhaust duct was used. The off-plane contribution of the body forces were modelled by an axisymmetric azimuthal velocity component (ANSYS INC 2019). For the 3D implementation an azimuthal section equivalent to the extend one blade passage (16.36^o) was used. For both approaches the computational domain is extended from a point near the spinner tip to a plane near the exhaust throat (Figure 4). For the present work, only clean inlet flows were available for the validation.
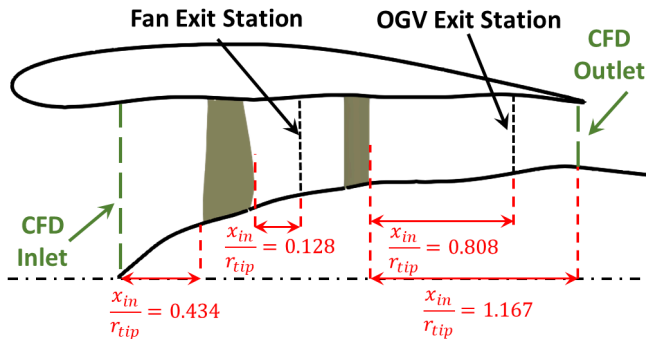

FIGURE 4: NASA Rotor 4 (Hughes 2002) geometry with relative measurement rake locations

A steady viscous compressible flow CFD approach is used with the k-ω SST turbulence model. The hub and the shroud are defined as no-slip, non-conductive walls with a y^+ value near unity. The inlet boundary condition is set as a total pressure inlet matching the wind tunnel (Hughes 2002) conditions. A static pressure outlet is used to model the outlet of the domain (Figure 4). The target fan flow capacity the static pressure at the outlet was modified. Periodic rotational boundary conditions are used for the lateral faces of the domain on the sector 3D approach. To model the effect of the fan blade tip gap, the source terms are set to zero on that region.

As a higher order numerical reference, the stage performance of the R4 was evaluated by a steady mixing plane approach. The blade and the vane domains are generated independently, and their interaction is modelled with a mixing plane model with an interpolation of the boundary values. The k-ω SST model is used as the turbulence model. A tip gap of 0.15% of the fan blade radius is used. A total pressure inlet boundary condition was imposed at the domain inlet to match the reference wind tunnel (Hughes 2002) boundary conditions. Rotational periodic boundary conditions were applied for the blade and the vane side domains. Target inlet capacity for each fan rotation speed is modelled by changing the static pressure value at the vane outlet. A mixing plane approach with a mixed-out averaging method (ANSYS INC 2019) is used to map the blade domain outlet with the vane domain inlet. Non-conducting, non-slip boundary conditions were applied for the domain wall surfaces. The OGV domain hub, shroud and vane, and the

blade shroud walls were modelled as static elements. A relative rotation matching the fan rotation speed value is applied for the blade walls and the blade domain hub boundary.

The methodology defined by Celik et al. (2008) was used to determine the independence of the meshes applied in the validation . As the reference, for a fixed capacity at the Ω/Ω_{max}=70% fan speed one operation point defined with a fixed static pressure at the outlet is applied. Through the comparison of three refinement levels for each approach, the finest meshes were selected for the 3D-sector BFM (1.22×10^6) and the 2D-axisymmetric (7.56×10^4) approaches with a GCI of the 0.027% and the 0.09% for the temperature ratio and a 0.197% and a 0.12% for the stage pressure ratio. The second finest mesh was selected for the mixing plane model (1.93×10^6 for a single blade, 4.46×10^5 for a single vane) after achieving a satisfactory GCI value with a 0.025% and a 0.154% for the stage pressure and temperature ratio, respectively. For a full annulus definition of the fan stage, the 3D low order model requires less than a 40% of the number of mesh elements of the equivalent mixing plane model, and the 2D axisymmetric case requires only 0.11% of the mixing plane mesh size.

3.2. Stage performance

The fan stage pressure ratio, PR, and the total-to-total isentropic efficiency, η_{is}, were obtained for four fan rotational speeds ($\Omega/\Omega_{max} = 50 - 70 - 87.5 - 100\%$) for different inlet capacity, Q, values (Figs. 5-6). The 2D-axisymmetric and 3D sector BFM approaches are compared against the R4 experimental results (Hughes 2002), and the mixing plane model. The results are sampled using an area-weighted-average at the designated measure locations – fan exit station and OGV exit station (Figure 4) – following the reference experimental results. As defined in Hughes (2002), total temperature values are taken at the fan exit station and no total temperature losses are assumed at the OGV. Total pressure values are sampled at the OGV exit station. The mass flow is computed at the numerical domain inlet boundary and is normalized as the capacity, Q, with the reference inlet conditions and the fan face area.

An adequate agreement with the stage PR and η_{is} results is observed for all the approaches. The discrepancy on the stage pressure ratio between the numerical approaches and the experiments increases when the operation point moves towards the surge limit (Figure 5). The maximum discrepancy on the stage operation pressure ratio is observed for the $\Omega/\Omega_{max} = 100\%$ operation line, with an average difference with the experimental results of the 1.65% for the 3D Sector BFM, a 1.2% for the mixing plane model, and a 1.11% for the 2D-axisymmetric BFM. A larger discrepancy of the isentropic efficiency is observed for the BFM 3D Sector and the mixing plane approaches compared with the 2D axisymmetric approach for higher rotational speeds ($\Omega/\Omega_{max} = 87.5 - 100\%$). The rise in discrepancy of the stage performance from the experiments with the increase of the fan rotational speed is due to the increase of the Mach number, with transonic effects from the $\Omega/\Omega_{max} = 87.5\%$ operation line upwards Hughes (2002). In the near peak efficiency point, the difference of the 3D sector BFM approach with the experimental results is 0.63% at $\Omega/\Omega_{max} = 87.5\%$, and 1.44% at $\Omega/\Omega_{max} = 100\%$.

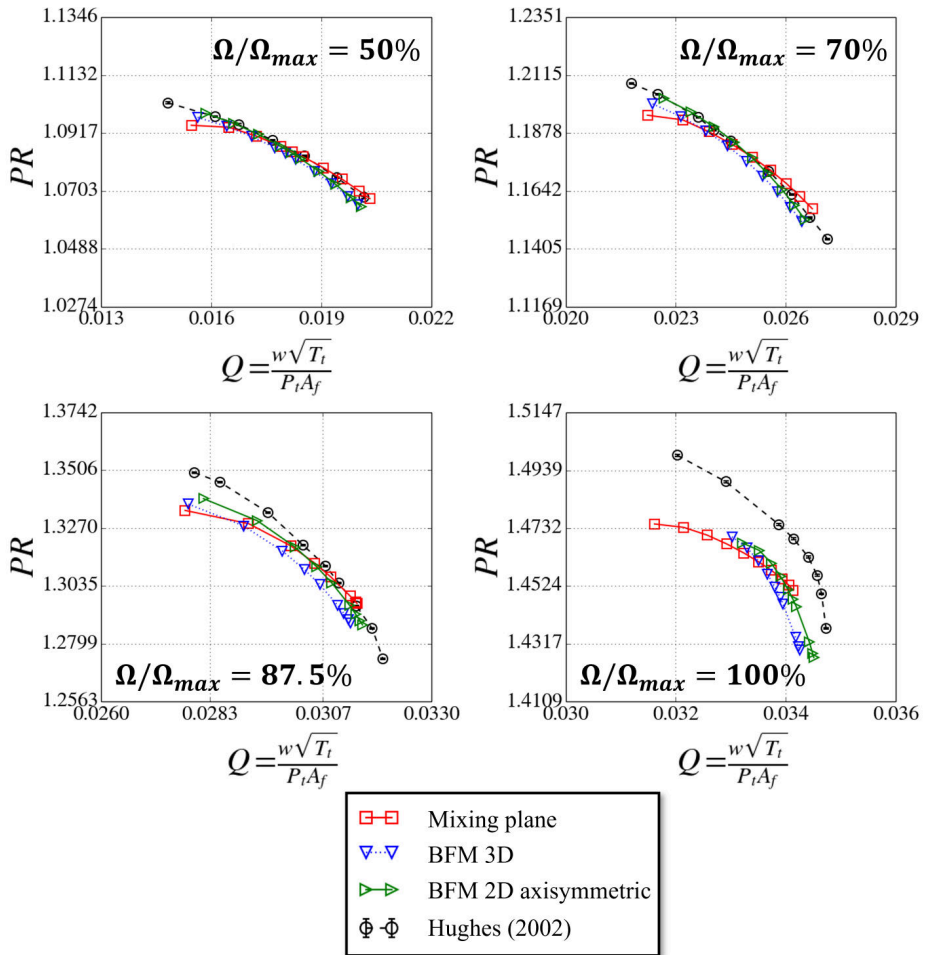Overall, the agreement of the model with the experimental results at different opera-

FIGURE 5: Stage Pressure Ratio (PR) of the NASA-R4 at 50-70-87.5-100% max rpm operation line. Experimental data from Hughes (2002)

tion speeds is considered sufficient to model preliminary aero-engine installation aerodynamics and provides a reasonable representation of the stage performance when compared with a higher order approach such as the mixing plane model.

3.3. Blade radial profiles

The radial distributions of the pressure ratio, total-to-total isentropic efficiency, and swirl angle were measured at the fan exit station (Figure 4) at the nominal operation points for Ω/Ω_{max}=87.5% and 100% (Hughes et al. 2013). At these conditions, the fan is operating at Q=0.02845 and Q=0.033, respectively. Each radial probe is circumferentially averaged using an area-weighted approach. A total of 25 equal area distributed probes are used for the sample.

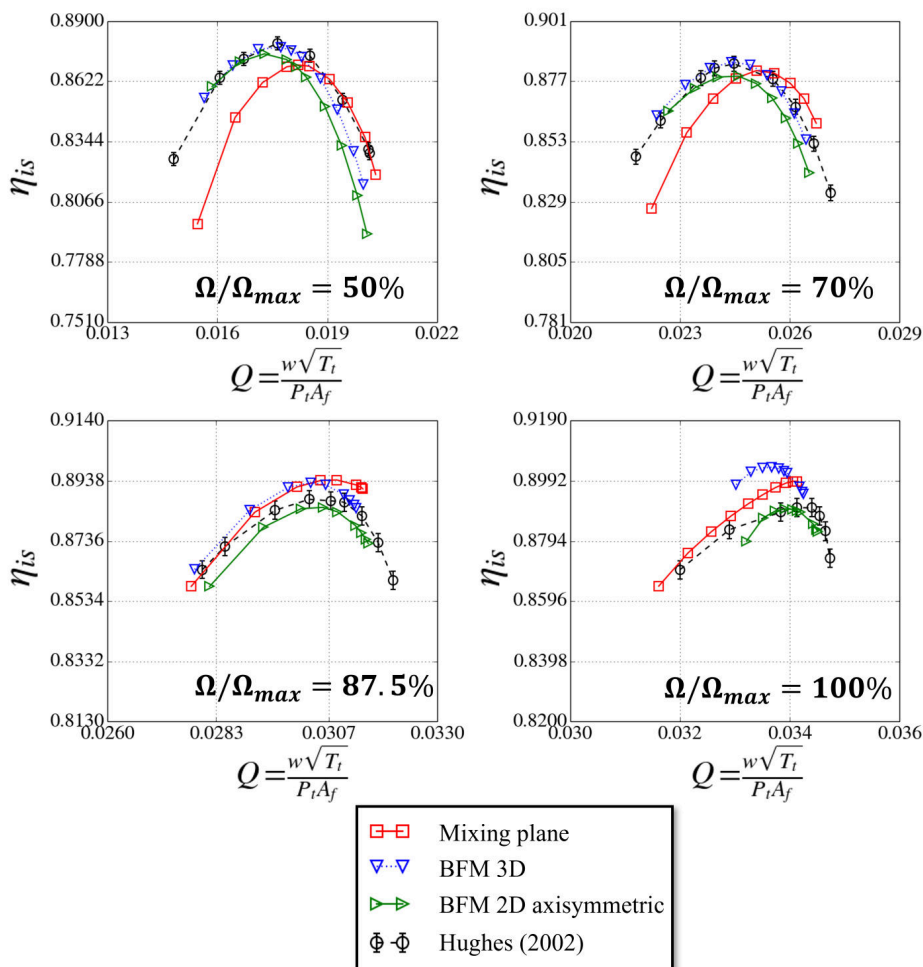Overall, the radial distributions of pressure ratio, isentropic efficiency, and swirl an-

FIGURE 6: Stage isentropic efficiency (η_{is}) of the NASA-R4 at 50-70-87.5-100% max rpm operation line. Experimental data from Hughes (2002)

gle are in reasonable agreement with the experimental results for both the mixing plane and the BFM approaches (Figure 7). The discrepancy in the radial distributions on the selected metrics increase on the near tip region over 80% of the blade span. This indicates that the BFM approaches do not fully characterize the flow turning in that region and mass flow rate. This results in a misrepresentation of the work distribution. Additionally, the increase of the relative velocity over the 80% of the span leads to the emergence of transonic flow induced losses that are not fully captured by the model. These loses lead to a local rise on the differences with the experiments on the isentropic efficiency radial distributions of the two BFM approaches. However, these discrepancies with the experiments and the mixing plane approach are considered sufficiently small for a lower order model such as the Hall-Thollet BFM. Hence, the model provides an adequate representation of the turbomachinery throughflow in cases where some loss in the accuracy is permitted

(A) Fan stage data $\Omega/\Omega_{max} = 87.5\%$, $Q = 0.02845$

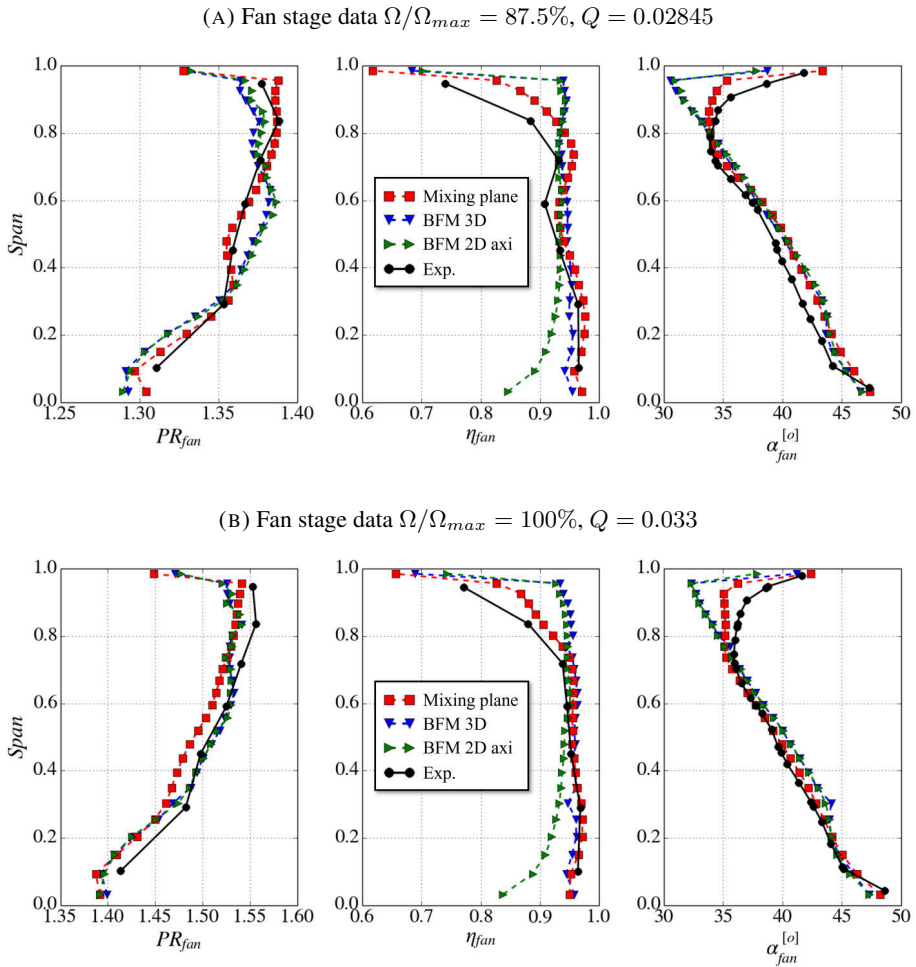(B) Fan stage data $\Omega/\Omega_{max} = 100\%$, $Q = 0.033$

FIGURE 7: NASA R4 normal operation point fan exit station pressure ratio, isentropic efficiency, and swirl angle radial profiles: (a) 87.5% max rpm operation line, and (b) 100% max rpm operation line. Experimental results from Hughes et al. (2013)

in favour of a reduction of the computational cost. For example, in comparison with the mixing plane approach, the 3D BFM required a 40% of the computational cost, while for the 2D axisymmetric BFM only a 0.11% of the computational cost was needed.

4. Optimization of the exhaust system of an aft mounted propulsor

4.1. Configuration sizing

The dimensions of the propulsive system are determined by the mid-cruise conditions of the propulsive system and the boundary layer ingestion requirements (Table 2). The amount of boundary layer ingested is defined by the Boundary Layer Ingestion Rate

(Equation 32), BLR. The BLR represents the ingested fraction of the boundary layer thickness at the fuselage reference station (Figure 2). The BLR value was chosen from the exchange between the mass flow requirement and the amount of momentum flux deficit ingested (Welstead & Felder 2016) to reduce the propulsor dimensions. The fan face area requirements is obtained to provide the target capacity of the fan for the selected BLR. In the present work, the propulsor is located axially at $l_{aft} = 3.45 \cdot r_{fus}$ (Figure 1). A hub-to-tip ratio of 0.3 is defined to maintain consistency with the R4 geometry. The dimensions and rotational speed of the fan were scaled for the operation conditions using the similitude principle (Dixon & Hall 2013). The compressibility calibration terms of the parallel force on the Hall-Thollet model (Equation 27) are dimension dependent through the relative velocity contribution to the local deviation angle (Equation 24). To simplify the scaling of the fan under this conditions and avoid additional calibration, the compressibility correction of the parallel force term is not applied on the present study. Nevertheless, when these terms are neglected the change on the stage efficiency with the variation of the Reynolds number are still accounted through the friction losses.

$$BLR = \frac{h_{BLI}}{\delta_{99}} \tag{32}$$

Cycle parameter	Value	Unit
FPR	~1.3	-
Ω/Ω_{max}	87.5	(%)
Altitude	32,000	ft
M_∞	0.78	-
BLR	0.4	-

TABLE 2

Sample mid-cruise operating conditions.

4.2. *Exhaust geometry design space exploration*

The study of the performance of an embedded propulsive system requires the evaluation of several aerodynamic performance metrics. The closer integration of the propulsion system within the airframe increases the effect of the aerodynamic coupling between the different housing components. A possible consequence of this is the higher dependence of the different performance metrics to variations on the propulsion integration design. A design space exploration (DSE) was proposed to quantify the sensitivities of the performance metrics to the exhaust system design.

The close integration of the propulsive system implies that changes on the fan cowl afterbody flow distribution can affect the exhaust performance and operation requirements (Matesanz-García et al. 2020). Hence, to provide an adequate representation of the system performance the exhaust system cannot be studied in isolation. To account for the exhaust-nacelle coupling, the nacelle afterbody geometry was included on the exhaust geometry DSE while the forebody and the remaining housing components geometries were fixed
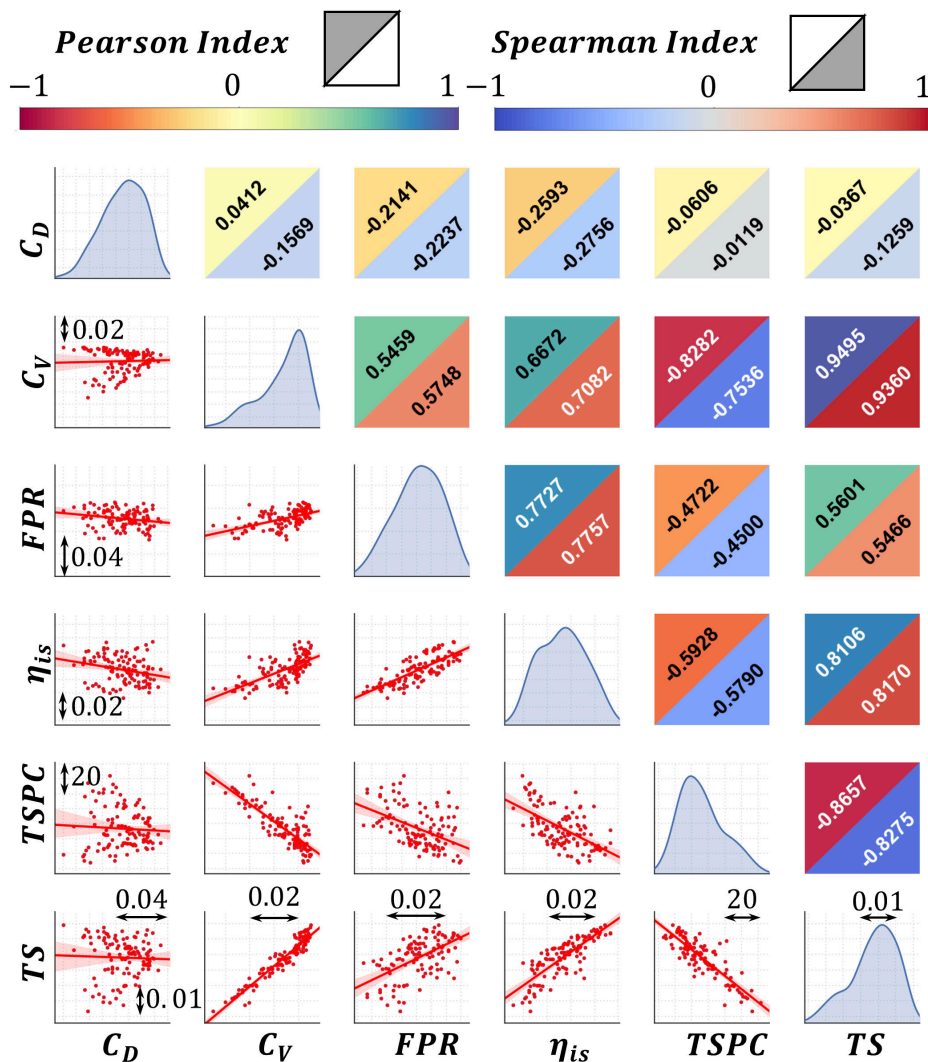
FIGURE 8: Exhaust and nacelle afterbody design space exploration: correlation between the system and the exhaust performance metrics

from a baseline. The changes on the exhaust and nacelle afterbody designs will affect the turbomachinery performance through changes on operation mass flow rate. These changes are driven by the variation on the exhaust effective areas and the changes on the discharge static pressure driven by the nacelle afterbody flow topology. Thus, the fan pressure ratio (FPR) and isentropic efficiency (η_{is}) have to be evaluated in conjunction with the thrust performance ($TSPC$, TS) and the exhaust performance metrics (C_D, C_V).

A DSE of the nacelle afterbody and the exhaust geometry was performed. A Latin Hypercube Sampling (LHS) approach is used to provide an even population of the design space (Tejero et al. 2021). The aft-fuselage, intake, turbomachinery domain, and nacelle forebody geometries were kept constant. Sample mid-cruise operating conditions (Table

2) were used. For the geometry definition, 9 geometry parameters (Figure 1) were used as degrees of freedom (l_{nac}, r_{te}, β_{nac}, β_{noz}, A_{noz}, $\theta_{up,noz}$, $\theta_{down,noz}$, β_{cone}, and f_{crop}). The designs of the nacelle afterbody were filtered to maintain a monotonic curvature variation (Matesanz-García et al. 2020). The intersection between the nacelle and exhaust surfaces was also filtered. The designs with flow separation on the nacelle afterbody were also removed. The initial sample of the LHS was adjusted to obtain 144 valid designs after filtering.

The exhaust performance metrics (C_V and C_D), the turbomachinery performance metrics (FPR and η_{is}), and the propulsion integration aerodynamic performance metrics (TS and $TSPC$) were evaluated on the DSE data (Figure 8). The Pearson and Spearman indices are used to evaluate the correlation and the monotonicity of the selected metrics. The correlation and monotonicity are used to identify the independent performance metrics of the case. This will reduce the number of candidate objective functions required for a multi-objective optimization (MOO).

A very strong negative correlation (Taylor 1997) and monotonicity was observed between the propulsive integration performance metrics (TS and $TSPC$), with Pearson and Spearman indices higher than -0.8. This is a result of their definition were the only variation between the metrics is provided by the W_{prop} (Matesanz-García et al. 2020). Also, a very strong positive correlation and monotonicity between the TS and the C_V is observed, with Pearson and Spearman indices over 0.93. These correlation and their polarity means that for the three metrics (TS, $TSPC$, and C_V) only one will be required in the context of an optimization. The turbomachinery performance metrics (FPR and η_{is}) have a strong correlation (Pearson index 0.77), but when compared with the other metrics (TS, $TSPC$, and C_V) moderate levels of correlation and monotonicity are observed. However, under this context the correlation between TS and FPR can be considered sufficient to reduce the number of performance metrics on the study. Hence, both turbomachinery performance metrics (η_{is} and FPR) could be replaced by the TS in the context of an optimization. The discharge coefficient (C_D) has a not significant correlation and monotonicity with the other metrics of the study. Hence, it cannot be removed from the analysis of the exhaust performance.

4.3. *Multi-objective optimization*

The discharge coefficient (C_D) and the thrust split (TS) are required to quantify the exhaust performance and the thrust contribution of the embedded propulsor, respectively. These metrics are independent and have to be considered in parallel for the design of the exhaust system of the embedded propulsor. Thus, a multi-objective optimization (MOO) approach with CFD in the loop is required for the design of the exhaust and nacelle afterbody geometries of the embedded propulsion system.

Evolutionary algorithms and particle swarm algorithms have been successfully applied for MOO of the propulsion integration design of conventional under-wing podded engines. Sanchez Moreno et al. (2022) compared the performance of evolutionary algorithms NSGA-II (Deb et al. 2002) and IBEA (Zitzler & Künzli 2004) and the particle swarm algorithm OMOPSO (Reyes Sierra & Coello Coello 2005) for the optimisation

of nacelle aerodynamics for conventional wing-mounted engines. This work indicated a higher robustness on convergence rate with the application of OMOPSO in comparison with the evolutionary algorithms. IBEA also had a better performance than NSGA-II. Based on Sanchez Moreno et al. (2022), an independent test was carried to evaluate these MOO algorithms for the propulsion integration design of embedded propulsive systems with the methodology presented in this work. IBEA provided a higher robustness and convergence rate than OMOPSO and NSGA-II for the aerodynamic optimisation of the aft-mounted BLI propulsor. Thus, the Indicator-Based Evolutionary Algorithm (IBEA) (Zitzler & Künzli 2004) is used in this work. The indicator metric of the optimization was the Hypervolume Index (Zitzler & Thiele 1999). Two objective functions to maximize are selected (Equation 33) based on the candidate functions of the DSE (Figure 8). Nine degrees of freedom are used based on the geometry parametrization (Figure 1). The DSE populated by the Latin Hypercube Sampling is used as a seed. Further 45 generations of maximum 36 individuals each are applied. The number of generations and individuals was adjusted based on the work of Robinson (2018). Each generation was evaluated with 6 simultaneous CFD processes in 240 CPUs. Including the mesh generation and post-processing, the optimisation process required approximately 4.5 days. The convergence is addressed with the Hypervolume Index (HV). A variation of the HV of less than the 0.01% on the last 5 generations is obtained. To filter the aerodynamic performance, the designs that present flow separation on the nacelle afterbody are removed from the optimization. Continuous curvature rate at the nacelle afterbody and no intersection between the nacelle and the exhaust geometries are enforced.

$$\begin{matrix} Objective \\ functions \end{matrix} : \begin{cases} maximize\,(TS) \\ maximize\,(C_D) \end{cases} \tag{33}$$
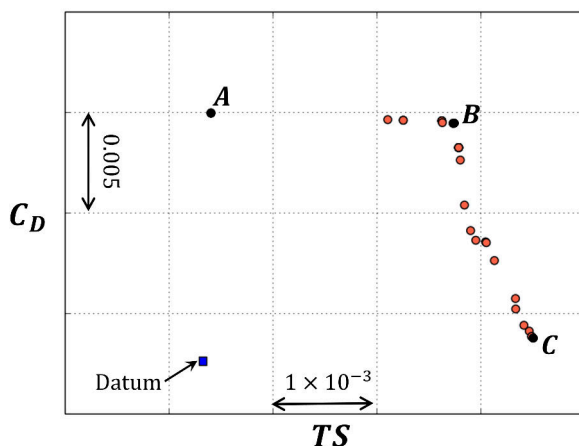

FIGURE 9: Pareto front of the exhaust design multi-objetive optimization

The non-dominated designs of the MOO result on a two-dimensional Pareto front (Figure 9). Three reference non-dominated designs were selected to understand the limits of the design space. Additionally, a datum exhaust design is included to compare the

design requirements (Figure 9). The non-dominated designs of the Pareto front extend on a range of approximately 0.3% of the total required thrust of the aircraft and a 1.5% of the discharge coefficient. However, near the maximum C_D values the variation of the discharge coefficient is negligible when compared with the variation of the TS. This is a consequence of the choked flow in the exhaust (Figure 10). Under this condition, the mass flow on the exhaust remains constant and the variations on the maximum C_D between non-dominated designs are defined by the effective static pressure at the discharge plane. Hence, there is no substantial reduction on the exhaust discharge losses between the non-dominated design A and the non-dominated design B (Figure 9), while a benefit of approximately 0.22% on the maximum TS can be obtained by the application of the non-dominated design B. The effective static pressure variation at the exhaust discharge is defined by the flow diffusion on the nacelle afterbody. The rise on the afterbody diffusion increases the effective nozzle pressure ratio (λ_{eff}). The increase on λ_{eff} chokes the exhaust for specific non-dominated designs (Figure 10). Under this condition, the discharge coefficient value cannot increase more for a given exhaust design. For an embedded propulsor, the variation on the exhaust static pressure is more relevant than on a conventional podded exhaust. This is due to the effect of the fuselage boundary layer that adds a higher variation to the static pressure over the cowl compared with the freestream value.
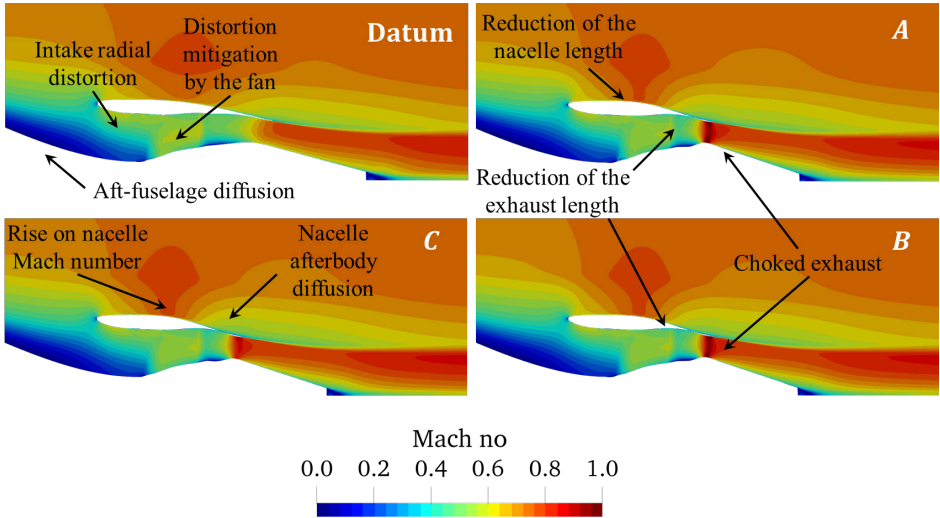

FIGURE 10: Mach number contours of the selected non-dominated designs (Figure 9) compared with the datum design

A manually designed Datum design (Figure 10) was introduced to compare with the non-dominated designs of the Pareto front (Figure 9). This design was conceived for a smooth curvature variation on the nacelle afterbody with an unchoked convergent nozzle. A notable improvement on the TS and C_D values can be obtained from the Datum design by the application of any of the non-dominated designs. A maximum benefit of 0.32% in TS can be obtained with design C. The increase on the TS is mainly driven by the

reduction of the system length with shorter exhaust ducts and length of the cone (Figure 10). The reduction of the exhaust duct length reduces the nacelle afterbody length (l_{nac}) of the proposed experiment (Figure 11). This reduces the cowl wetted area and the drag contribution of the propulsion integration. An additional thrust contribution is obtained by the reduction of the nacelle trailing edge radius, r_{te} (Figure 11). Thus, there is a potential benefit on the application of compact exhaust systems on the aft mounted embedded propulsor.

The reduction on the trailing edge radial position combined with the shorter nacelle afterbody increases the flow expansion on the aft nacelle but at the same time increases the pressure force contribution with the change on the surface normal. Additionally, for similar exhaust throat areas, the change on r_{te} moves the radial position of the cone downwards. The lower radial position of the cone reduces the drag contribution of the surface, but the cone angle (β_{cone}) has to be adjusted to maximize the thrust contribution of the expansion of the nozzle exhaust flow (Figure 11). Hence, the nacelle afterbody design has a notable effect on the thrust operation and defines the exhaust operation conditions.
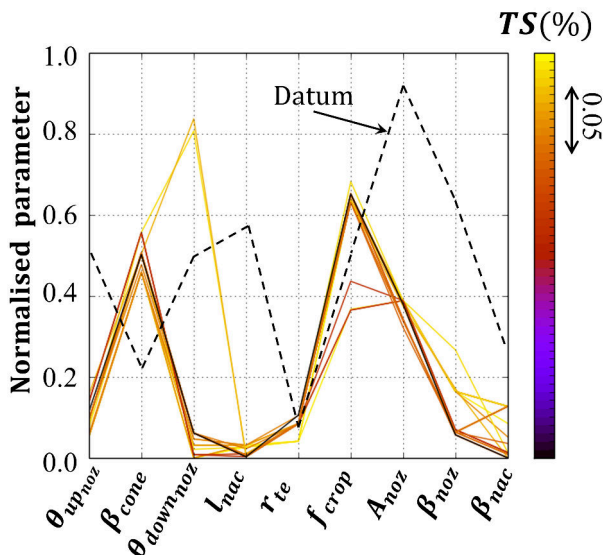

FIGURE 11: Parallel coordinates plot of the non-dominated designs of the Pareto front for the nine degrees of freedom

An increase between 1.25% and 1.19% of C_D from the Datum configuration can be obtained with designs A and B, respectively (Figure 9). However, a considerable penalty on the TS is found for the design A compared with the B (0.3%). This is indicative of the importance of the exhaust design on embedded systems. While a reduction of the exhaust length and trailing edge radial position is observed for all the configurations on the Pareto front (Figure 11), the other design parameters can outweigh the benefit of the more compact system. Hence, the application of more compact exhaust designs for the embedded propulsive system will require detailed design of the exhaust characteristics to maximize the aerodynamic performance.

5. Conclusion

A methodology for the optimization of the aerodynamic design of the exhaust system of close-coupled propulsive systems has been defined. The methodology is based on a 2D axisymmetric definition of an aft-mounted BLI annular propulsor. A parametric definition of the geometry is coupled with an automated meshing and CFD approach.

A throughflow body force model has been implemented to model the turbomachinery response to the distortion. The implementation of such model has been validated against the NASA Rotor 4 geometry for 2D and 3D applications. The numerical approaches show reasonable agreement with the stage pressure ratio characteristics across the fan map. The discrepancy with the experimental results increases slightly on the direction of the surge limit, and with the increase of the fan rotational speed. An adequate agreement with the experiments was found for the radial distributions of pressure ratio, isentropic efficiency and swirl angle. The discrepancies with the experiments increased on the near tip region. Therefore, the low order model provides an adequate representation of the turbomachinery throughflow in cases where some loss in the accuracy is permitted in favour of a reduction of the computational cost (40% of computational cost for 3D BFM and 0.11% for 2D BFM compared with mixing plane reference).

A multi-objective optimization methodology was applied for the exhaust and nacelle afterbody geometries. The indicator-based evolutionary algorithm (IBEA) is used with the presented design methodology in the loop. To select the objective functions between the different metrics of interest a design space exploration is performed. Strong correlations were found between the exhaust design metrics and the thrust performance. After the evaluation of the correlation between the different metrics the problem was reduced to two objective functions.

The non-dominated designs of the multi-objective optimization are used to identify the main requirements for an embedded propulsor exhaust design. A potential benefit on the thrust performance was identified by the application of more compact exhaust systems (0.32% of the total thrust required by the aircraft). However, it was observed that the change of some of the detail design parameters could outweigh the benefits achieved by the bulk reduction of the exhaust length. Hence, the design of these compact exhaust systems requires of a detailed design of the geometry.

Additionally, the nacelle afterbody design was observed to have a notable impact on the exhaust operation. More compact nacelle afterbody designs can increase the effective nozzle pressure ratio and change the exhaust operation point. The embedded propulsive systems are more susceptible to changes on the effective nozzle pressure ratio than the conventional podded propulsors. This is due to the effect of the boundary layer on the external static pressure. Under these conditions, relatively small changes on the nacelle afterbody can lead to relevant changes on the effective nozzle pressure ratio. Thus, it is necessary to consider the effect of the nacelle afterbody to define the exhaust operating conditions.

References

ANSYS INC (2019), ANSYS Fluent User's Guide. Release 19.1, Technical report, ANSYS Inc, Canonsburg, PA, USA.
URL: *ansyshelp.ansys.com*

Benichou, E., Dufour, G., Bousquet, Y., Binder, N., Ortolan, A. & Carbonneau, X. (2019), 'Body force modeling of the aerodynamics of a low-speed fan under distorted inflow', *International Journal of Turbomachinery, Propulsion and Power* **4**(3).

Celik, I. B., Ghia, U., Roache, P. J., Freitas, C. J., Coleman, H. & Raad, P. E. (2008), 'Procedure for estimation and reporting of uncertainty due to discretization in CFD applications', *Journal of Fluids Engineering, Transactions of the ASME* **130**(7), 0780011–0780014.

Christie, R., Robinson, M., Tejero, F. & MacManus, D. G. (2019), 'The use of hybrid intuitive class shape transformation curves in aerodynamic design', *Aerospace Science and Technology* **1**, 105473.
URL: *https://doi.org/10.1016/j.ast.2019.105473*

Dae Kim, H. (2010), 'Distributed Propulsion Vehicles', *27th International Congress of the Aeronautical Sciences, ICAS 2010* pp. 1–11.
URL: *https://ntrs.nasa.gov/archive/nasa/casi.ntrs.nasa.gov/20100036222.pdf*

Deb, K., Member, A., Pratap, A., Agarwal, S. & Meyarivan, T. (2002), 'A fast and elitist multi-objective genetic algorithm:NSGAII', **6**(2), 182–197.

Defoe, J. J., Etemadi, M. & Hall, D. K. (2018), 'Fan performance scaling with inlet distortions', *Journal of Turbomachinery* **140**(7), 1–11.

Dixon, S. L. & Hall, C. (2013), *Fluid Mechanics and Thermodynamics of Turbomachinery*, 7th edn, Elsevier.

Gohardani, A. S., Doulgeris, G. & Singh, R. (2011), 'Challenges of future aircraft propulsion: A review of distributed propulsion technology and its potential application for the all electric commercial aircraft', *Progress in Aerospace Sciences* **47**(5), 369–391.

Goulos, I., MacManus, D. & Sheaf, C. (2019), 'Civil turbofan engine exhaust aerodynamics: Impact of fan exit flow characteristics', *Aerospace Science and Technology* **93**, 105181.
URL: *https://doi.org/10.1016/j.ast.2019.05.033*

Goulos, I., Stankowski, T., Otter, J., MacManus, D., Grech, N. & Sheaf, C. (2016), 'Aerodynamic Design of Separate-Jet Exhausts for Future Civil Aero-engines - Part I: Parametric Geometry Definition and Computational Fluid Dynamics Approach', *Journal of Engineering for Gas Turbines and Power* **138**(8), 1–14.

Gunn, E. J., Tooze, S. E., Hall, C. A. & Colin, Y. (2013), 'An experimental study of loss sources in a fan operating with continuous inlet stagnation pressure distortion', *Journal of Turbomachinery* **135**(3).

Habermann, A. L., Gokhale, A. & Hornung, M. (2021), 'Numerical investigation of the effects of fuselage upsweep in a propulsive fuselage concept', *CEAS Aeronautical Journal* **12**(1), 173–189.
URL: *http://link.springer.com/10.1007/s13272-020-00487-2*

Habermann, A. L., Zahn, R., Seitz, A. & Hornung, M. (2020), Multidimensional Parametric Study of a Propulsive Fuselage Concept Using OpenFOAM. AIAA 2020-2754, *in* 'AIAA AVIATION 2020 FORUM', American Institute of Aeronautics and Astronautics, VIRTUAL EVENT.
URL: *https://arc.aiaa.org/doi/10.2514/6.2020-2754*

Hall, D. K. (2015), Analysis of civil aircraft propulsors with boundary layer ingestion, Phd thesis, Massachusetts Institute of Technology.
URL: *https://dspace.mit.edu/handle/1721.1/97353*

Hall, D. K., Huang, A. C., Uranga, A., Greitzer, E. M., Drela, M. & Sato, S. (2017), 'Boundary layer ingestion propulsion benefit for transport aircraft', *Journal of Propulsion and Power* **33**(5), 1118–1129.

Hughes, C. E. (2002), 'Aerodynamic Performance of Scale-Model Turbofan Outlet Guide Vanes Designed for Low Noise', *40th AIAA Aerospace Sciences Meeting & Exhibit - Cleveland , OH* .
URL: *https://arc.aiaa.org/doi/abs/10.2514/6.2002-374*

Hughes, C. E., Woodward, R. P., Podboy, G. G. & Jeracki, R. J. (2013), The effect of bypass nozzle exit area on fan aerodynamic performance and noise in a model turbofan simulator, *in* 'Proceedings of the ASME Turbo Expo', Vol. 6 PART B, pp. 1241–1264.

Kim, H. & Liou, M. S. (2017), 'Flow simulation and optimal shape design of N3-X hybrid wing body configuration using a body force method', *Aerospace Science and Technology* .

Lee, B. J., Liou, M.-F., Celestina, M. & To, W. (2020), Benefit and Critical Factors for the Performance of the Boundary Layer Ingesting Propulsion, *in* 'Volume 2A: Turbomachinery', American Society of Mechanical Engineers, pp. 1–16.
URL: *https://asmedigitalcollection.asme.org/GT/proceedings/GT2020/84065/Virtual, Online/1094441*

Lee, B. J., Liou, M.-F. & Liou, M.-S. (2018), Conceptual Aerodynamic Design of a Tail-Cone Thruster System Under Axi-Symmetric Inlet Distortion, *in* 'Volume 2A: Turbomachinery', American Society of Mechanical Engineers, pp. 1–17.
URL: *https://asmedigitalcollection.asme.org/GT/proceedings/GT2018/50992/Oslo, Norway/289852*

Matesanz-García, J., Christie, R., Tejero, F., MacManus, D. & Heidebrecht, A. (2020), 'An automated approach for the aerodynamic design of close-coupled propulsion/airframe configurations', *1st Aerospace Europe Conference, Bordeaux, France* .

MIDAP Study group (1979), Guide to in-Flight Thrust Measurement of Turbo- jets and Fan Engines. Agardograph No. 237, Technical Report No. AG-237, Technical report, AGARD (Advisory Group for Aerospace Research and Development), Neuilly sur Seine, France.

Milea, A.-S. (2020), Aero-engine installation aerodynamics and design for novel aircraft configurations - MSc Thesis, Msc thesis, Cranfield University.

Reyes Sierra, M. & Coello Coello, C. A. (2005), 'Improving PSO-based Multi-Objective optimization using crowding, mutation and ϵ-dominance', *Lecture Notes in Computer Science* **3410**, 505–519.

Robinson, M. H. (2018), The Aerodynamics of Aero-Engine Nacelles, Phd thesis, Cranfield University.

Sanchez Moreno, F., MacManus, D., Tejero, F., Matesanz-García, J. & Sheaf, C. (2022), Robustness of optimisation algorithms for transonic aerodynamic design, *in* '9th European Conference for Aeronautics and Space Sciences (EUCASS-3AF 2022)', Lille, France.

Sanders, D. (2018), Boundary Layer Ingestion Performance Assessment with Application to Bussines Jets, Phd thesis, Cranfield University.

Seitz, A., Habermann, A. L. & van Sluis, M. (2020), 'Optimality considerations for propulsive fuselage power savings', *Jornal of Aerospace Engineering* .

Steiner, H.-J., Seitz, A., Wieczorek, K., Plötner, K., Isikveren, A. & Hornung, M. (2012), Multi-disciplinary Design and Feasibility Study of Distributed Propulsion Systems. 2012-1.7.5, *in* '28th Congress of the International Council of the Aeronautical Sciences 2012, ICAS 2012', American Institute of Aeronautics and Astronautics.

Taylor, J. R. (1997), *An introduction to Error Analysis: The study of uncertainties in physical measurements*, Mill Valley, Calif University Science Books.

Tejero, F., Christie, R., MacManus, D. & Sheaf, C. (2021), 'Non-axisymmetric aero-engine nacelle design by surrogate-based methods', *Aerospace Science and Technology* **117**, 106890.
URL: *https://linkinghub.elsevier.com/retrieve/pii/S1270963821004004*

Tejero, F., Matesanz-García, J., Swarthout, A. & MacManus, D. (2022), Towards the design and optimisation of future compact aero-engines: intake/fancowl trade-off investigation. FP04-AER, *in* '56th 3AF International Conference on Applied Aerodynamics', 3AF: Association Aéronautique et Astronautique de France, Toulouse, France.

Thollet, W. (2017), Body force modeling of fan – airframe interactions, Phd thesis, ISAE-SUPAERO, Toulouse, France.

Valencia, E. A., Nalianda, D., Laskaridis, P. & Singh, R. (2015), 'Methodology to assess the performance of an aircraft concept with distributed propulsion and boundary layer

ingestion using a parametric approach', *Proceedings of the Institution of Mechanical Engineers, Part G: Journal of Aerospace Engineering* **229**(4), 682–693.

Welstead, J. & Felder, J. L. (2016), Conceptual Design of a Single-Aisle Turboelectric Commercial Transport with Fuselage Boundary Layer Ingestion, *in* '54th AIAA Aerospace Sciences Meeting', American Institute of Aeronautics and Astronautics, San Diego, California, pp. 1–17.
URL: *http://arc.aiaa.org/doi/10.2514/6.2016-1027 https://arc.aiaa.org/doi/10.2514/6.2016-1027*

Wiart, L., Atinault, O., Grenon, R., Paluch, B. & Hue, D. (2015), 'Development of NOVA Aircraft Configurations for Large Engine Integration Studies', *33rd AIAA Applied Aerodynamics Conference* (June), 1–30.
URL: *http://arc.aiaa.org/doi/10.2514/6.2015-2254*

Zitzler, E. & Künzli, S. (2004), 'Indicator-based selection in multiobjective search', *Lecture Notes in Computer Science (including subseries Lecture Notes in Artificial Intelligence and Lecture Notes in Bioinformatics)* **3242**, 832–842.

Zitzler, E. & Thiele, L. (1999), 'Multiobjective evolutionary algorithms: A comparative case study and the strength Pareto approach', *IEEE Transactions on Evolutionary Computation* **3**(4), 257–271.